

# An Ocean Circulation Model Based on Operator-Splitting, Hamiltonian Brackets, and the Inclusion of Sound Waves

RICK SALMON

*Scripps Institution of Oceanography, University of California, San Diego, La Jolla, California*

(Manuscript received 28 August 2008, in final form 30 January 2009)

## ABSTRACT

This paper offers a simple, entirely prognostic, ocean circulation model based on the separation of the complete dynamics, including sound waves, into elementary Poisson brackets. For example, one bracket corresponds to the propagation of sound waves in a single direction. Other brackets correspond to the rotation of the velocity vector by individual components of the vorticity and to the action of buoyancy force. The dynamics is solved by Strang splitting of the brackets. Key features of the method are the assumption that the sound waves propagate exactly one grid distance in a time step and the use of Riemann invariants to solve the sound-wave dynamics exactly. In these features the method resembles the lattice Boltzmann method, but the flexibility of more conventional methods is retained. As in the lattice Boltzmann method, very short time steps are required to prevent unrealistically strong coupling between the sound waves and the slow hydrodynamic motions of primary interest. However, the disadvantage of small time steps is more than compensated by the model's extreme simplicity, even in the presence of very complicated boundaries, and by its massively parallel form. Numerical tests and examples illustrate the practicality of the method.

## 1. Introduction

This paper offers a simple, completely prognostic, numerical ocean circulation model based on the full equations of fluid dynamics, including sound waves. Simplicity is achieved by splitting the dynamics into a sequence of elementary steps. For example, one step corresponds to the propagation of sound waves in, say, the  $x$  direction. Another step corresponds to the action of Coriolis force. Each step corresponds to a Hamiltonian bracket; hence, important conservation laws survive. Because the model dynamics includes sound waves, there is no need to solve any elliptic boundary value problems. All dependent variables step forward in time. This greatly facilitates the coding, especially in complicated geometry. In fact, the complete model comprises a relatively large number of very short subroutines, which because of directional splitting, are actually indifferent to the complexity of the ocean basin shape.

The sound speed is an adjustable parameter of the model and need not be as large as the actual sound

speed. The only general requirement is that the Mach number be small compared to unity. In rotating flow, the acoustic deformation radius,  $c/f$  (sound speed divided by Coriolis parameter), must be larger than the domain size. In stratified flow, the scale depth,  $c/N$  (sound speed divided by Väisälä frequency), must be larger than the ocean depth. By choosing the time step to be the gridpoint separation divided by the sound speed, we solve the “sound-wave split” exactly, using the method of Riemann invariants. Thus, small time steps correspond to large sound speed and to realistically incompressible flow.

Two earlier papers (Salmon 1999a,b) entertained the idea of solving ocean circulation models using the lattice Boltzmann method. Unfortunately, subsequent attempts to apply the lattice Boltzmann method to ocean basins with realistic bathymetry failed for reasons connected with the inflexibility of the method and with the highly anisotropic nature of ocean dynamics—the huge dissimilarity between leading-order dynamical balances in the horizontal and vertical directions. At the same time, more recent work (Salmon 2004, 2005, 2007) has re-emphasized the importance of retaining conservation laws in numerical algorithms. The present method, which attempts to combine the advantages of the lattice

---

*Corresponding author address:* Rick Salmon, UCSD Dept. 0213, 9500 Gilman Drive, La Jolla, CA 92093-0213.  
E-mail: rsalmon@ucsd.edu

Boltzmann method with the need to maintain conservation laws, represents a marriage of these two philosophies. In the lattice Boltzmann method, fluid particles hop from one grid point to the next in a time step. In the method of this paper, Riemann invariants propagate exactly one grid distance in a time step. However, whereas lattice Boltzmann particles relax irreversibly (and hence diffusively) toward a local equilibrium state that represents the entire dynamics, our propagation of Riemann invariants is but one component—one split—of the complete dynamics. We solve each of the splits by an algorithm that is designed especially for that split and maintains as many conservation laws as possible.

No matter what the method, viscosity and diffusion must be present to represent subgrid-scale physics. However, the viscous and diffusive splits should not affect the conservative nature of the others. Unlike in the lattice Boltzmann method—or, for that matter, the more widely used “semi-Lagrangian” advection schemes—our viscosity and diffusion are independent, separately controllable, components of the whole dynamics.

The plan of the paper is as follows: Section 2 introduces the basic physics in Hamiltonian form and explains the fundamental analytical approximation, a modification of the Hamiltonian that simplifies the dynamics but still accurately corresponds to the Boussinesq equations in the limit  $c \rightarrow \infty$  of infinite sound speed. Since we make no approximation to the Poisson bracket, the analytical equations preserve all the exact conservation laws. A partition of the Poisson bracket into three parts produces rotation subdynamics, sound-wave subdynamics, and buoyancy subdynamics. Each of these subdynamics is applied separately to the flow using Strang splitting. We solve the sound-wave subdynamics (section 3) by directional splitting and the use of Riemann invariants. Buoyancy subdynamics (section 4) also uses directional splitting, with the precise formulation selected for its compatibility with the sound-wave subdynamics and with the conservation of mass, buoyancy, and buoyancy squared. The latter may be especially important because it, along with total energy conservation, guarantees the conservation of the sum of kinetic, internal, and *available* potential energy. Rotation subdynamics (section 5) does not use directional splitting but instead splits the  $\boldsymbol{\omega} \times \mathbf{v}$  term into pieces proportional to the three components of the vorticity  $\boldsymbol{\omega}$ . Section 6 compares solutions of our model in two horizontal dimensions to solutions obtained using more conventional methods.

All ocean circulation models face fundamental difficulties associated with the huge disparity between the horizontal and vertical spatial resolution. Section 7 explains how one solution to this problem—the “aspect

ratio trick” proposed by Browning et al. (1990)—is ideally suited to the present method; it corresponds to an adjustment to the sound speed that equates the time required for sound waves to propagate a vertical grid distance to the time required to propagate a horizontal grid distance. Section 8 presents solutions of ocean convection over realistic topography that incorporate this aspect-ratio trick. Section 9 concludes.

## 2. Analytical approximations

We begin with the perfect-fluid equations in the form

$$\frac{\partial \mathbf{v}}{\partial t} = \mathbf{v} \times \boldsymbol{\omega} - \nabla \left( \frac{1}{2} \mathbf{v} \cdot \mathbf{v} + c^2 \rho / \rho_0 \right) + \theta \mathbf{k}, \quad (2.1a)$$

$$\frac{\partial \rho}{\partial t} = -\nabla \cdot (\rho \mathbf{v}), \quad (2.1b)$$

and

$$\frac{\partial \theta}{\partial t} = -\mathbf{v} \cdot \nabla \theta, \quad (2.1c)$$

where  $\mathbf{v}$  is the fluid velocity;  $\boldsymbol{\omega} = \nabla \times \mathbf{v} + 2\boldsymbol{\Omega}$  is the total vorticity, including the earth’s rotation vector  $\boldsymbol{\Omega}$ ;  $\rho$  is the mass density with representative constant value  $\rho_0$ ;  $c$  is the sound speed (a prescribed constant); and  $\theta$  is the buoyancy, which could be further subdivided into temperature and salinity. The “exact” dynamics (2.1) are equivalent to the Hamiltonian bracket formulation,

$$\frac{dF}{dt} = \{F, H_e\}, \quad (2.2)$$

where  $F = F[\mathbf{v}, \rho, \theta]$  is any functional of the variables  $\mathbf{v}(x, y, z, t)$ ,  $\rho(x, y, z, t)$ , and  $\theta(x, y, z, t)$ ;  $\{F, H_e\}$  is the Poisson bracket defined by

$$\begin{aligned} \{F, H_e\} = & \iiint d\mathbf{x} \frac{\boldsymbol{\omega}}{\rho} \cdot \left( \frac{\delta F}{\delta \mathbf{v}} \times \frac{\delta H_e}{\delta \mathbf{v}} \right) \\ & + \iiint d\mathbf{x} \left( \nabla \frac{\delta F}{\delta \rho} \cdot \frac{\delta H_e}{\delta \mathbf{v}} - \nabla \frac{\delta H_e}{\delta \rho} \cdot \frac{\delta F}{\delta \mathbf{v}} \right) \\ & + \iiint d\mathbf{x} \frac{\nabla \theta}{\rho} \cdot \left( \frac{\delta F}{\delta \mathbf{v}} \frac{\delta H_e}{\delta \theta} - \frac{\delta H_e}{\delta \mathbf{v}} \frac{\delta F}{\delta \theta} \right) \end{aligned} \quad (2.3)$$

and

$$H_e = \iiint d\mathbf{x} \left( \frac{1}{2} \rho \mathbf{v} \cdot \mathbf{v} + \frac{1}{2} \frac{c^2}{\rho_0} \rho^2 - \rho \theta z \right) \quad (2.4)$$

is the exact Hamiltonian. By successively setting  $F = \mathbf{v}(\mathbf{x}_0)$ ,  $\rho(\mathbf{x}_0)$ ,  $\theta(\mathbf{x}_0)$ , where  $\mathbf{x}_0$  is an arbitrary fixed location, and making use of the functional derivatives

$$\frac{\delta H_e}{\delta \mathbf{v}} = \rho \mathbf{v}; \quad \frac{\delta H_e}{\delta \rho} = \frac{1}{2} \mathbf{v} \cdot \mathbf{v} + c^2 \rho / \rho_0 - \theta z; \quad \frac{\delta H_e}{\delta \theta} = -\rho z, \quad \frac{\delta F}{\delta \mathbf{v}} = \frac{\delta F}{\delta \mathbf{v}}; \quad \frac{\delta F}{\delta \rho} = \frac{c^2}{\rho_0} \left( \frac{\delta F}{\delta \phi} + \frac{\alpha \delta F}{\phi \delta \alpha} \right); \quad \frac{\delta F}{\delta \theta} = \frac{\phi \delta F}{c^2 \delta \alpha}. \quad (2.5) \tag{2.10}$$

we recover the exact dynamics (2.1). Strictly speaking, the bracket (2.3) applies only to unbounded flow; the incorporation of boundary conditions into Poisson brackets is problematic. However, we use (2.3) only to infer the governing finite-difference equations within the fluid interior. We infer the corresponding boundary conditions by requiring that the appropriate fluxes vanish at boundaries.

Now we introduce approximations, both analytical and numerical, to the Poisson bracket (2.3) and the Hamiltonian (2.4). Our single analytical approximation will be to replace the exact Hamiltonian  $H_e$  by

$$H = \iiint d\mathbf{x} \left( \frac{1}{2} \rho_0 \mathbf{v} \cdot \mathbf{v} + \frac{1}{2} \frac{c^2}{\rho_0} \rho^2 - \rho \theta z \right) \quad (2.6)$$

in which the constant average density replaces the density factor in the kinetic-energy term. We make no analytical approximations to the bracket. Since now

$$\frac{\delta H}{\delta \mathbf{v}} = \rho_0 \mathbf{v}; \quad \frac{\delta H}{\delta \rho} = c^2 \rho / \rho_0 - \theta z; \quad \frac{\delta H}{\delta \theta} = -\rho z, \quad (2.7)$$

we obtain the approximate dynamics

$$\frac{\partial \mathbf{v}}{\partial t} = \frac{\rho_0}{\rho} \mathbf{v} \times \boldsymbol{\omega} - \nabla(c^2 \rho / \rho_0) + \theta \mathbf{k}, \quad (2.8a)$$

$$\frac{\partial \rho}{\partial t} = -\nabla \cdot (\rho_0 \mathbf{v}), \quad (2.8b)$$

and

$$\frac{\partial \theta}{\partial t} = -\frac{\rho_0}{\rho} \mathbf{v} \cdot \nabla \theta. \quad (2.8c)$$

The advantage of (2.6) over (2.4) is that it leads to Eqs. (2.8), in which the sound waves move at an absolutely constant speed. This makes it possible to solve the sound-wave split exactly. In the limit  $c \rightarrow \infty$  of interest, both the exact dynamics (2.1) and the approximate dynamics (2.8) reduce to the Boussinesq equations, despite the difference between (2.1a) and (2.8a).

To pave the way for numerical approximations, we introduce the new variables

$$\phi \equiv c^2 \frac{\rho}{\rho_0}; \quad \alpha \equiv \frac{\rho}{\rho_0} \theta \quad (2.9)$$

and transform the variables from  $(\mathbf{v}, \rho, \theta)$  to  $(\mathbf{v}, \phi, \alpha)$ . The functional derivatives transform as

Hence, (2.3) and (2.6) take the forms

$$\frac{dF}{dt} = \{F, H\}_1 + \{F, H\}_2 + \{F, H\}_3, \quad (2.11)$$

where

$$\{F, H\}_1 = \iiint d\mathbf{x} \frac{c^2}{\phi} \boldsymbol{\omega} \cdot \left( \frac{\delta F}{\delta \mathbf{v}} \times \frac{\delta H}{\delta \mathbf{v}} \right), \quad (2.12a)$$

$$\{F, H\}_2 = c^2 \iiint d\mathbf{x} \left( \nabla \frac{\delta F}{\delta \phi} \cdot \frac{\delta H}{\delta \mathbf{v}} - \nabla \frac{\delta H}{\delta \phi} \cdot \frac{\delta F}{\delta \mathbf{v}} \right), \quad (2.12b)$$

$$\{F, H\}_3 = c^2 \iiint d\mathbf{x} \frac{\alpha}{\phi} \left( \nabla \frac{\delta F}{\delta \alpha} \cdot \frac{\delta H}{\delta \mathbf{v}} - \nabla \frac{\delta H}{\delta \alpha} \cdot \frac{\delta F}{\delta \mathbf{v}} \right), \quad (2.12c)$$

and

$$H = \iiint d\mathbf{x} \left( \frac{1}{2} \mathbf{v} \cdot \mathbf{v} + \frac{1}{2} \frac{\phi^2}{c^2} - \alpha z \right). \quad (2.13)$$

(Note that a factor of  $\rho_0$  has been cancelled between the brackets and the Hamiltonian.) The advantage of the transformation (2.9) is that (2.12c) takes a simpler form than the last term in (2.3).

The three brackets in (2.12) correspond, respectively, to the rotation subdynamics

$$\frac{\partial \mathbf{v}}{\partial t} = \{\mathbf{v}, H\}_1 = \frac{c^2}{\phi} \mathbf{v} \times \boldsymbol{\omega}, \quad (2.14a)$$

$$\frac{\partial \phi}{\partial t} = \{\phi, H\}_1 = 0, \quad (2.14b)$$

$$\frac{\partial \alpha}{\partial t} = \{\alpha, H\}_1 = 0; \quad (2.14c)$$

the sound-wave subdynamics

$$\frac{\partial \mathbf{v}}{\partial t} = \{\mathbf{v}, H\}_2 = -\nabla \phi, \quad (2.15a)$$

$$\frac{\partial \phi}{\partial t} = \{\phi, H\}_2 = -c^2 \nabla \cdot \mathbf{v}, \quad (2.15b)$$

$$\frac{\partial \alpha}{\partial t} = \{\alpha, H\}_2 = 0; \quad (2.15c)$$

and the buoyancy subdynamics

$$\frac{\partial \mathbf{v}}{\partial t} = \{\mathbf{v}, H\}_3 = c^2 \frac{\alpha}{\phi} \mathbf{k} = \theta \mathbf{k}, \quad (2.16a)$$

$$\frac{\partial \phi}{\partial t} = \{\phi, H\}_3 = 0, \quad (2.16b)$$

$$\frac{\partial \alpha}{\partial t} = \{\alpha, H\}_3 = -c^2 \nabla \cdot \left( \frac{\alpha}{\phi} \mathbf{v} \right) = -\nabla \cdot (\mathbf{v}\theta). \quad (2.16c)$$

We obtain approximate dynamics equivalent to (2.8) by summing up the terms on the rhs of (2.14), (2.15), and (2.16). However, we solve the dynamics (2.14)–(2.16) by applying each of the three subdynamics, (2.14), (2.15), and (2.16) successively, at each time step. In fact, we further split each subdynamics into its directional or vorticity components, as described in following sections. In the limit  $c \rightarrow \infty$ , both the exact dynamics (2.1) and approximate dynamics (2.14)–(2.16) reduce to the Boussinesq equations

$$\frac{\partial \mathbf{v}}{\partial t} = \mathbf{v} \times \boldsymbol{\omega} - \nabla \phi + \theta \mathbf{k}, \quad (2.17a)$$

$$\nabla \cdot \mathbf{v} = 0, \quad (2.17b)$$

$$\frac{\partial \theta}{\partial t} = -\mathbf{v} \cdot \nabla \theta \quad (2.17c)$$

for incompressible flow. Thus, our entire procedure is merely a device for solving (2.17).

We replace each subdynamics by finite-difference analogs that maintain as many conservation laws as possible. The energy (2.13) is conserved or semiconserved as long as the spatial discretization maintains the antisymmetry property of each of the brackets in (2.12). By “semiconservation,” we mean conservation except for errors in the discretization of the time derivative. Besides the energy, we also wish to conserve the mass

$$M = \iiint d\mathbf{x} \phi \propto \iiint d\mathbf{x} \rho, \quad (2.18)$$

the buoyancy

$$B = \iiint d\mathbf{x} \alpha \propto \iiint d\mathbf{x} \rho \theta, \quad (2.19)$$

and the squared buoyancy

$$Z = \frac{1}{2} \iiint d\mathbf{x} \frac{\alpha^2}{\phi} \propto \iiint d\mathbf{x} \rho \theta^2. \quad (2.20)$$

Additional conserved quantities include the momentum (disregarding the effects of solid boundaries and the buoyancy force)

$$\mathbf{P} = \iiint d\mathbf{x} \phi \mathbf{v} \propto \iiint d\mathbf{x} \rho \mathbf{v}, \quad (2.21)$$

the integrated potential vorticity

$$Q = \iiint d\mathbf{x} \phi q \propto \iiint d\mathbf{x} \boldsymbol{\omega} \cdot \nabla \theta, \quad (2.22)$$

and the potential enstrophy

$$Q_2 = \iiint d\mathbf{x} \phi q^2 \propto \iiint d\mathbf{x} (\boldsymbol{\omega} \cdot \nabla \theta)^2 \rho^{-1}, \quad (2.23)$$

where  $q = \boldsymbol{\omega} \cdot \nabla \theta / \rho$  is the Ertel potential vorticity conserved on fluid particles. The approximate dynamics (2.14)–(2.16) conserves all of (2.18)–(2.23) because the bracket (2.12) is exact and because the conservation of (2.18)–(2.23) depends only on the form of the bracket. (Although momentum conservation requires translation invariance of the Hamiltonian, the form of the conserved momentum depends only on the bracket (for a discussion of this point, see Shepherd 1990).

### 3. Sound-wave splitting

We discretize the sound-wave subdynamics by further splitting (2.15) into each direction. For example, the  $z$ -direction sound-wave dynamics is

$$\frac{\partial w}{\partial t} = -\frac{\partial \phi}{\partial z}, \quad (3.1a)$$

$$\frac{\partial \phi}{\partial t} = -c^2 \frac{\partial w}{\partial z}, \quad (3.1b)$$

$$\frac{\partial(\phi\theta)}{\partial t} = 0. \quad (3.1c)$$

Equations (3.1a) and (3.1b) form a closed system equivalent to

$$\frac{\partial}{\partial t} \left( w + \frac{\phi}{c} \right) + c \frac{\partial}{\partial z} \left( w + \frac{\phi}{c} \right) = 0;$$

$$\frac{\partial}{\partial t} \left( w - \frac{\phi}{c} \right) - c \frac{\partial}{\partial z} \left( w - \frac{\phi}{c} \right) = 0. \quad (3.2)$$

Once (3.2) are solved, (3.1c) determines  $\theta$  from the new value of  $\phi$ . Equations (3.2) can be solved exactly if the vertical grid spacing  $\Delta z$  is equal to  $c \Delta t$ , the sound velocity multiplied by the time step: that is, no matter how one chooses to interpolate between gridpoint values,

the solution is exact if both Riemann invariants translate exactly one grid distance. In an unbounded domain, the exact solution is

$$\left(w + \frac{\phi}{c}\right)_i^{n+1} = \left(w + \frac{\phi}{c}\right)_{i-1}^n; \quad \left(w - \frac{\phi}{c}\right)_i^{n+1} = \left(w - \frac{\phi}{c}\right)_{i+1}^n, \tag{3.3}$$

where superscripts denote the time step and subscripts denote the vertical grid location. The two Riemann invariants are shifted right and left. If a solid bottom boundary is present at, for example, grid point 1, then the boundary condition  $w = 0$  there implies that

$$\left(w + \frac{\phi}{c}\right)_0^n = -\left(w - \frac{\phi}{c}\right)_2^n. \tag{3.4}$$

This provides the recipe for reflecting one Riemann invariant into the other. An analogous condition holds at the upper rigid boundary. At interior grid points, (3.3) corresponds to the finite difference formulas

$$w_i^{n+1} = \frac{1}{2}(w_{i-1}^n + w_{i+1}^n) + \frac{1}{2c}(\phi_{i-1}^n - \phi_{i+1}^n) \tag{3.5a}$$

and

$$\phi_i^{n+1} = \frac{1}{2}(\phi_{i-1}^n + \phi_{i+1}^n) + \frac{c}{2}(w_{i-1}^n - w_{i+1}^n); \tag{3.5b}$$

while at the lower boundary we have

$$w_1^{n+1} = 0 \tag{3.6a}$$

and

$$\phi_1^{n+1} = \phi_2^n - c w_2^n. \tag{3.6b}$$

Since  $c = \Delta z/\Delta t$ , (3.5) and (3.6) are logical finite-difference approximations. It is easy to verify that (3.5) and (3.6) conserve an approximation to the mass in the form

$$\frac{1}{2}\phi_1 + \phi_2 + \phi_3 + \dots \tag{3.7}$$

and an approximation to the energy in the form [cf. (2.13)]

$$0 + \frac{w_2^2}{2} + \frac{w_3^2}{2} + \dots + \frac{\phi_1^2}{4c^2} + \frac{\phi_2^2}{2c^2} + \frac{\phi_3^2}{2c^2} + \dots. \tag{3.8}$$

Note that the boundary points receive half the weight—represent half the volume—of the interior points.

Now let  $S_z(\Delta t)$  be the propagator corresponding to the  $z$ -direction sound-wave split just described; that is, if

$\psi(t)$  is any dependent variable, such as the value of  $w$  at a particular grid point, then  $\psi(t + \Delta t) = S_z(\Delta t)\psi(t)$  is its value after a time  $\Delta t = \Delta z/c$ , according to (3.5) and (3.6). [Note that  $S_z$  includes the exact, small change in  $\theta$  that arises from (3.1c) and the change in  $\phi$ .] Let  $S_x(\Delta t)$  and  $S_y(\Delta t)$  be the corresponding propagators for sound-wave propagation in the  $x$  and  $y$  direction, respectively. For the moment, we assume that the grid spacing is the same in all directions; an alternative will be considered in section 7. Then the algorithm

$$\psi(t + 2\Delta t) = S_x(\Delta t)S_y(\Delta t)S_z(\Delta t)S_z(\Delta t)S_y(\Delta t)S_x(\Delta t)\psi(t) \tag{3.9}$$

corresponding to sound-wave propagation in the  $x$  direction for a time  $\Delta t$ , followed by  $y$ -direction propagation for a time  $\Delta t$ , followed by  $z$ -direction propagation, etc., is a logical approximation to evolution under the full, three-dimensional sound-wave subdynamics (2.15) for a time  $2\Delta t$ . The pyramidal arrangement (3.9) is called Strang splitting and is well known to yield a result that is second-order accurate in time (see, e.g., Durran 1999, 130–132). Even more accurate splitting methods are known (e.g., Suzuki 1992), but these require time steps that are not multiples of one another and cannot, therefore, take advantage of our Riemann-invariant method for exactly solving the directional splits. Since each directional split conserves energy, mass, and momentum, the composite algorithm (3.9) also conserves these quantities.

Our complete numerical algorithm will be a generalization of (3.9) that contains splits representing the remaining subdynamics (2.14) and (2.16) (as well as splits containing the forcing and dissipation). However, the errors caused by Strang splitting of (2.14) and (2.16) are small compared to the errors in (3.9) because the rotation and buoyancy subdynamics evolve much more slowly than the sound waves. Thus, it makes sense to analyze (3.9) by itself.

To see how (3.9) works in the presence of boundaries, consider the two-dimensional domain shown in Fig. 1. The solid lines represent solid boundaries, and the dashed lines are “propagation lines” along which either  $S_x$  or  $S_y$  is applied. The propagation lines lie wholly within the fluid; nowhere is a propagation line tangent to a boundary. The boundary conditions, analogous to (3.6), assume that each propagation line intersects the boundary in a locally normal direction. Thus, the boundary is poorly resolved at sharp corners where two perpendicular propagation lines intersect. In the inviscid case, segments of the boundary with many sharp corners generate grid-scale sound waves. However, if the Mach number is sufficiently small, then the energy converted to sound waves in this way is negligible. The

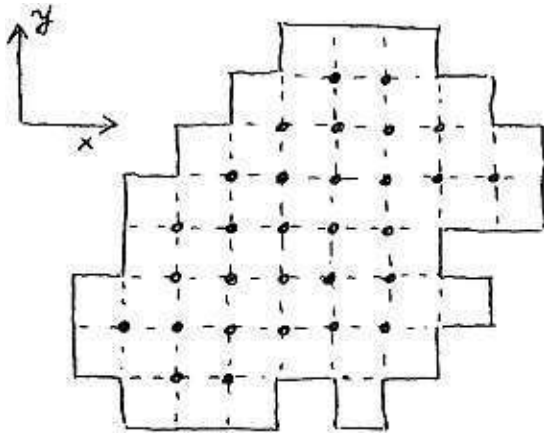


FIG. 1. Propagation lines for sound waves in a bounded domain. The waves propagate along the dashed lines through the interior of the fluid. Both components of the fluid velocity vanish at the boundary points.

resulting small-scale oscillations, chiefly visible in the pressure field, have little effect on the much slower “hydrodynamic” motions of primary interest.

The introduction of viscosity and no-slip boundary conditions further reduces the generation of grid-scale sound waves at rough boundaries. In the viscous case, the boundary conditions described above are closely analogous to the “bounce back” boundary conditions corresponding to no-slip boundary conditions in lattice Boltzmann theory. Experiments show that the spuriously generated sound waves largely disappear if the

viscous boundary layer thickness is at least several grid distances wide. Of course, one could also overcome boundary roughness by either rounding or shaving the corners in Fig. 1, but this would couple the sound waves propagating in perpendicular directions—greatly complicating our simple scheme.

For a more quantitative analysis of the sound-wave splitting, we consider unbounded flow in two spatial dimensions. Letting  $u(x, y, t) = U(t) \exp[i(kx + ly - \omega t)]$ , etc., we define the state vector  $\Psi(t) \equiv [U(t), V(t), \Phi(t)/c]^T$ . Then the sound-wave propagators  $S_x(t)$  and  $S_y(t)$  correspond to the matrices

$$S_x(t) = \begin{bmatrix} \cos(ckt) & 0 & -i \sin(ckt) \\ 0 & 1 & 0 \\ -i \sin(ckt) & 0 & \cos(ckt) \end{bmatrix}$$

and

$$S_y(t) = \begin{bmatrix} 1 & 0 & 0 \\ 0 & \cos(ctl) & -i \sin(ctl) \\ 0 & -i \sin(ctl) & \cos(ctl) \end{bmatrix}. \quad (3.10)$$

The approximation

$$\Psi(t) = S_x(t/2)S_y(t)S_x(t/2)\Psi(0) \quad (3.11)$$

is the two-dimensional analog of (3.9). On the other hand, the exact solution of (2.15) in two dimensions is  $\Psi(t) = S(t)\Psi(0)$ , where

$$S(t) = \frac{1}{K^2} \begin{bmatrix} k^2 \cos(cKt) + l^2 & kl(\cos(cKt) - 1) & -ikK \sin(cKt) \\ kl(\cos(cKt) - 1) & k^2 + l^2 \cos(cKt) & -ilK \sin(cKt) \\ -ikK \sin(cKt) & -ilK \sin(cKt) & K^2 \cos(cKt) \end{bmatrix} \quad (3.12)$$

is the exact propagator. Here  $K = \sqrt{k^2 + l^2}$ . All of the matrices in (3.10) and (3.12) are unitary matrices, corresponding to the fact that the energy is conserved.

Now, if either  $k = 0$  or  $l = 0$ , then (3.11) is exact because  $S_x$  and  $S_y$  are exact. To investigate the worst possible case, we therefore set  $k = l$ , corresponding to a wave vector directed at a 45° angle to the coordinate directions. In this case,

and

$$S_x(\Delta t) = \begin{bmatrix} \cos(\gamma) & 0 & -i \sin(\gamma) \\ 0 & 1 & 0 \\ -i \sin(\gamma) & 0 & \cos(\gamma) \end{bmatrix}$$

$$S_y(\Delta t) = \begin{bmatrix} 1 & 0 & 0 \\ 0 & \cos(\gamma) & -i \sin(\gamma) \\ 0 & -i \sin(\gamma) & \cos(\gamma) \end{bmatrix}, \quad (3.13)$$

where  $\gamma = ck\Delta t = k\Delta x$  ranges between 0 and  $\pi$ . For this same wave, the exact propagator (3.12) is

$$S(2\Delta t) = \frac{1}{2} \begin{bmatrix} \cos(2\sqrt{2} \gamma) + 1 & \cos(2\sqrt{2} \gamma) - 1 & -i\sqrt{2} \sin(2\sqrt{2} \gamma) \\ \cos(2\sqrt{2} \gamma) - 1 & \cos(2\sqrt{2} \gamma) + 1 & -i\sqrt{2} \sin(2\sqrt{2} \gamma) \\ -i\sqrt{2} \sin(2\sqrt{2} \gamma) & -i\sqrt{2} \sin(2\sqrt{2} \gamma) & 2 \cos(2\sqrt{2} \gamma) \end{bmatrix}. \quad (3.14)$$

Thus, in this worst-case situation, the approximation (3.11) replaces (3.14) by the product

$$\begin{bmatrix} \cos(\gamma) & 0 & -i \sin(\gamma) \\ 0 & 1 & 0 \\ -i \sin(\gamma) & 0 & \cos(\gamma) \end{bmatrix} \begin{bmatrix} 1 & 0 & 0 \\ 0 & \cos(2\gamma) & -i \sin(2\gamma) \\ 0 & -i \sin(2\gamma) & \cos(2\gamma) \end{bmatrix} \begin{bmatrix} \cos(\gamma) & 0 & -i \sin(\gamma) \\ 0 & 1 & 0 \\ -i \sin(\gamma) & 0 & \cos(\gamma) \end{bmatrix}. \quad (3.15)$$

For well-resolved sound waves ( $\gamma \rightarrow 0$ ), (3.14) and (3.15) differ by terms  $O(\gamma^3)$ . However, for the worst-resolved waves near  $\gamma = \pi$ , the difference between (3.14) and (3.15) is significant. The exact propagator (3.14) corresponds to the two-dimensional form of (2.15), namely

$$\frac{\partial u}{\partial t} = -\frac{\partial \phi}{\partial x}, \quad \frac{\partial v}{\partial t} = -\frac{\partial \phi}{\partial y}; \quad \frac{\partial \phi}{\partial t} = -c^2 \left( \frac{\partial u}{\partial x} + \frac{\partial v}{\partial y} \right). \quad (3.16)$$

The eigenvalues of (3.14) are 1 and  $e^{\pm i2\sqrt{2}\gamma}$ , corresponding, respectively, to steady nondivergent flow and to sound waves propagating at the speed  $c$  in opposite directions. The approximate propagator (3.15) has one unit eigenvalue—corresponding to steady motion—at all values of the nondimensional wavenumber  $\gamma$ . However, the corresponding static eigenvector differs very significantly from the exact static eigenvector

$$\Psi \equiv [-1, +1, 0]^T \quad (3.17)$$

near the highest resolved wavenumber.

The ratio of the sound-wave speed implied by the approximation (3.15) to the exact value  $c$  implied by (3.14) is shown by curve A in Fig. 2. Although the sound speed of well-resolved waves with  $\gamma \ll 1$  is close to  $c$ , poorly resolved sound waves with  $\gamma > 1$  propagate at a speed that vanishes in the limit  $\gamma = \pi$  of the smallest resolved wavelength. Thus, all three eigenvalues of (3.15) approach unity as  $\gamma \rightarrow \pi$ , and the Strang-splitting approximation (3.15) misrepresents the smallest resolved sound waves as entirely static. Curve B in Fig. 2 is the fraction of energy in steady nondivergent flow represented by the exact static eigenvector (3.17) that is lost after two time steps of evolution by the approximate dynamics (3.15). At two poorly resolved wavenumbers, the energy in (3.17) is entirely drained in this short time.

Once again, this simple, linear analysis applies to the worst possible case of sound waves propagating at a 45° angle to the coordinate axes; waves propagating in the directions of the axes experience no errors at all. In the complete model, which must include viscosity, the most poorly resolved waves lie inside the dissipation range.

Nevertheless, our analysis suggests that Strang splitting of sound waves suffers from errors that spuriously couple the slow hydrodynamic motions of primary physical interest to unphysical small-scale motions with relatively large pressure fluctuations. The fully nonlinear numerical experiments described in section 6 support this suggestion, but the experiments show that the errors are small and easy to control. These errors, which result solely from the directional splitting, are the price to be paid for the stark simplicity of our method.

It is important to emphasize that one would never use our model to study sound waves any more than one would use the lattice Boltzmann method for that purpose. In both models the sound waves are fast modes that serve merely as a device for (approximately) enforcing the incompressibility condition while avoiding elliptic boundary value problems. Although we incorporate the remaining physics by a splitting method similar to that used for the sound waves, the remaining physics comprises slow hydrodynamic modes that are well resolved by the short time steps. As long as the sound speed is sufficiently large, there is no significant coupling between the sound waves and the slow hydrodynamic motions of primary physical interest. Of course, the most convincing assessment of our method is a direct comparison to more conventional methods with proven accuracy. We do this in section 6, but first we consider the additional splits corresponding to buoyancy and rotation subdynamics.

#### 4. Buoyancy splitting

In the buoyancy subdynamics (2.16),  $\mathbf{v}$  and  $\alpha$  evolve but  $\phi$  remains fixed. In contrast to (3.1), the directional splits of (2.16) cannot be solved exactly. Instead, we seek an algorithm that semiconserves energy, buoyancy (2.19), and its square (2.20). Since (2.20) involves  $\phi$  as well as  $\alpha$ , we must take the results of the previous section into account; that is, the conservation of buoyancy squared must be coordinated with the sound-wave split.

Again considering only the vertical direction, we first note that the previously derived sound-wave algorithm (3.5) corresponds to the spatial discretizations

$$\{F, H\}_2 = \frac{c^2}{2\Delta z} \sum_i \left[ \left( \frac{\partial F}{\partial \phi_{i+1}} - \frac{\partial F}{\partial \phi_i} \right) \left( \frac{\partial H}{\partial w_i} + \frac{\partial H}{\partial w_{i+1}} \right) - \left( \frac{\partial H}{\partial \phi_{i+1}} - \frac{\partial H}{\partial \phi_i} \right) \left( \frac{\partial F}{\partial w_i} + \frac{\partial F}{\partial w_{i+1}} \right) \right] \quad (4.1)$$

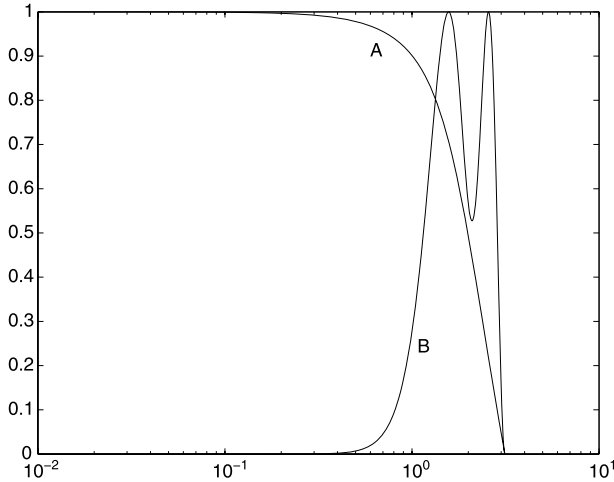


FIG. 2. Two measures of the error caused by Strang splitting of the propagators  $S_x$  and  $S_y$  in the worst-case situation of a wave vector pointing at a  $45^\circ$  angle to the grid. (a) The ratio of the sound speed to its exact value  $c$  as a function of the nondimensional wavenumber  $\gamma$ . The largest value  $\gamma = \pi$  corresponds to the most poorly resolved wave. (b) The fraction of the energy in steady nondivergent flow that is spuriously converted to sound waves in two time steps. No errors occur when the wave vector points in the  $x$  or  $y$  direction.

and

$$H = \frac{1}{2} \sum_{i=1}^{N-1} \left( \frac{w_i^2}{2} + \frac{w_{i+1}^2}{2} \right) + \left( \frac{\phi_i^2}{2c^2} + \frac{\phi_{i+1}^2}{2c^2} \right) - (\alpha_i z_i + \alpha_{i+1} z_{i+1}) \quad (4.2)$$

of (2.12b) and (2.13), where  $i = 1$  and  $i = N$  correspond to solid boundaries. Note that (4.2) gives boundary points half the weight of interior points. As previously stated, the bracket (4.1) applies only to unbounded flow. Thus, (4.1) and (4.2) imply the semidiscrete form

$$\frac{dw_i}{dt} = -\frac{(\phi_{i+1} - \phi_{i-1})}{2\Delta z}, \quad (4.3a)$$

$$\frac{d\phi_i}{dt} = -c^2 \frac{(w_{i+1} - w_{i-1})}{2\Delta z}, \quad (4.3b)$$

$$\frac{d(\phi_i \theta_i)}{dt} = 0 \quad (4.3c)$$

of the interior Eqs. (3.5), but not the semidiscrete form

$$\frac{dw_1}{dt} = 0; \quad \frac{d\phi_1}{dt} = -c^2 \frac{w_2}{\Delta z}; \quad \frac{d(\phi_1 \theta_1)}{dt} = 0 \quad (4.4)$$

of the boundary conditions (3.6).

For the discretization of the buoyancy bracket (2.12c), we take

$$\begin{aligned} \{F, H\}_3 &= \frac{c^2}{4\Delta z} \sum_i \left( \frac{\alpha_{i+1}}{\phi_{i+1}} + \frac{\alpha_i}{\phi_i} \right) \\ &\times \left[ \left( \frac{\partial F}{\partial \alpha_{i+1}} - \frac{\partial F}{\partial \alpha_i} \right) \left( \frac{\partial H}{\partial w_i} + \frac{\partial H}{\partial w_{i+1}} \right) \right. \\ &\quad \left. - \left( \frac{\partial H}{\partial \alpha_{i+1}} - \frac{\partial H}{\partial \alpha_i} \right) \left( \frac{\partial F}{\partial w_i} + \frac{\partial F}{\partial w_{i+1}} \right) \right]. \end{aligned} \quad (4.5)$$

Setting  $F = w_i, \phi_i, \alpha_i$  in (4.5) and making use of (4.2), we obtain the semidiscrete buoyancy subdynamics

$$\frac{dw_i}{dt} = \frac{1}{4} (\theta_{i-1} + 2\theta_i + \theta_{i+1}), \quad (4.6a)$$

$$\frac{d\phi_i}{dt} = 0, \quad (4.6b)$$

$$\begin{aligned} \frac{d}{dt} \left( \frac{\phi_i}{c^2} \theta_i \right) &= \frac{1}{4\Delta z} [(\theta_{i-1} + \theta_i)(w_{i-1} + w_i) \\ &\quad - (\theta_i + \theta_{i+1})(w_i + w_{i+1})], \end{aligned} \quad (4.6c)$$

where we have used the definition  $\alpha_i = \phi_i \theta_i / c^2$ . Like (4.3), the subdynamics (4.6) apply only at interior grid points  $1 < i < N$ . However, it is straightforward to show that (4.6) and the boundary equations

$$w_1 = 0; \quad \frac{d\phi_1}{dt} = 0; \quad \frac{d}{dt} \left( \frac{\phi_1}{c^2} \theta_1 \right) = \frac{1}{2\Delta z} [-(\theta_1 + \theta_2)w_2] \quad (4.7)$$

semiconservate the energy (4.2) and the buoyancy

$$\frac{1}{2} \phi_1 \theta_1 + \phi_2 \theta_2 + \phi_3 \theta_3 + \dots \quad (4.8)$$

It is only slightly harder to show that the combined dynamics (4.3), (4.4), (4.6), and (4.7) together semiconservate the buoyancy squared

$$\frac{1}{2} \phi_1 \theta_1^2 + \phi_2 \theta_2^2 + \phi_3 \theta_3^2 + \dots \quad (4.9)$$

The discrete bracket (4.5) was obtained using the Nambu-bracket method developed in Salmon (2005, 2007). For present purposes, it suffices merely to verify that (4.6) and (4.7) have the claimed conservation properties.

Now let  $T_z$  be the  $z$ -direction propagator corresponding to (4.6) and (4.7). (Strictly speaking,  $T_z$  remains undefined until we choose a particular time stepping algorithm for the buoyancy split. In the experiments described in sections 6 and 8 we use second-order Runge–Kutta.) Let  $T_x$

and  $T_y$  be the corresponding propagators in the  $x$  and  $y$  directions. These differ from  $T_z$  only in that no buoyancy force occurs in the horizontal analogs of (4.6a). We apply these three propagators along the same propagation lines as the three sound-wave propagators. The composition

$$\psi(t + 2\Delta t) = S_x S_y S_z T_x T_y T_z T_y T_x S_z S_y S_x \psi(t) \tag{4.10}$$

represents the combined sound-wave and buoyancy dynamics. In (4.10) each propagator acts for a time  $\Delta t$ , the time required for a sound wave to propagate a distance equal to the grid spacing. Each sound-wave propagator exactly conserves energy, mass, momentum, and buoyancy. Each buoyancy propagator semiconserves these same quantities. The full algorithm (4.10), which corresponds to the perfect-fluid dynamics without rotation or inertia, semiconserves these quantities as well as the buoyancy squared. To simulate the full Boussinesq dynamics, it only remains to devise the splits corresponding to rotation subdynamics (2.14).

### 5. Rotational splitting

The subdynamics (2.14), in which only the velocity  $\mathbf{v}$  evolves, conserves energy and momentum (mass, buoyancy, and buoyancy squared are also trivially conserved). However, the most efficient algorithm for (2.14) is one that abandons exact conservation of momentum. First, suppose that  $\phi \equiv c^2$  and that the relative vorticity is omitted from (2.12a). Then, taking  $\boldsymbol{\omega} = f\mathbf{k}$ , we find that (2.14a) reduces to

$$\frac{\partial u}{\partial t} = fv; \quad \frac{\partial v}{\partial t} = -fu, \tag{5.1}$$

which are exactly solvable as

$$\begin{aligned} u(t) &= u(0) \cos(ft) + v(0) \sin(ft), \\ v(t) &= v(0) \cos(ft) - u(0) \sin(ft). \end{aligned} \tag{5.2}$$

In this case, the full dynamics resembles “planetary geostrophic dynamics,” except that it retains the local time derivative  $\partial \mathbf{v} / \partial t$ . The solution (5.2) conserves energy because it corresponds to a length-preserving rotation of the velocity vector.

We solve the general case (2.14a) by three splits similar to (5.2). We define the vertical rotation propagator  $R_z$  by

$$\begin{aligned} u(t) &= u(0)C_z + v(0)S_z \\ v(t) &= v(0)C_z - u(0)S_z, \end{aligned} \tag{5.3}$$

where  $C_z$  and  $S_z$  are the approximations

$$C_z = \frac{1 - \frac{1}{4}\gamma^2}{1 + \frac{1}{4}\gamma^2}; \quad S_z = \frac{\gamma}{1 + \frac{1}{4}\gamma^2}; \quad \gamma \equiv t \omega_z(0) c^2 / \phi \tag{5.4}$$

to  $\cos(t \omega_z(0) c^2 / \phi)$  and  $\sin(t \omega_z(0) c^2 / \phi)$ , respectively, and  $\omega_z = f + \partial v / \partial x - \partial u / \partial y$  is the vertical component of the vorticity. The rational expressions (5.4) are faster to compute than the corresponding trigonometric functions. The solution (5.3) is an approximation because  $\omega_z$  evolves with the flow. However, (5.3) conserves energy exactly because  $C_z^2 + S_z^2 = 1$ . The finite difference approximation to  $\omega_z(0)$  is arbitrary; in practice, we use simple centered differences.

We solve the complete subdynamics (2.14) by a Strang composition of  $R_z$  and the propagators  $R_x$  and  $R_y$  corresponding to  $\omega_x$  and  $\omega_y$ , respectively. Each rotation split corresponds to a rotation of the velocity vector about a single component of the vorticity. Exact momentum conservation is lost because it involves a cancellation between the terms in  $R_x$ ,  $R_y$ , and  $R_z$ .

### 6. Two-dimensional experiments

In this section we compare solutions of the splitting algorithm described in previous sections to solutions computed by more conventional methods. Our algorithm is

$$S_x S_y R_z D_{xy} R_z S_y S_x, \tag{6.1}$$

where  $S_x$  and  $S_y$  are the sound-wave splits described in section 3,  $R_z$  is the vertical rotation split described in section 5, and  $D_{xy}$  is a split corresponding to the action of a Navier–Stokes-type eddy viscosity with viscosity coefficient  $\nu$ . All the splits except  $D_{xy}$  act for the time  $\Delta x / c$  required for a sound wave to propagate a horizontal grid distance  $\Delta x$  in either direction. At the apex of the Strang-splitting pyramid,  $D_{xy}$  acts for time  $2\Delta x / c$ . The complete sequence (6.1) corresponds to an evolution time of  $2\Delta x / c$ . For  $D_{xy}$  we use

$$u_{ij}(t + 2\Delta x / c) = \frac{u_{ij} + \alpha(u_{i-1,j} + u_{i+1,j} + u_{i,j-1} + u_{i,j+1})}{(1 + 4\alpha)} \tag{6.2}$$

and similarly for  $v_{ij}$ , where subscripts denote grid locations,  $\alpha = 2\nu / (c \Delta x)$ , and all variables on the right-hand side of (6.2) are evaluated at time  $t$ . In the limit  $c \rightarrow \infty$ , the dynamics (6.1) corresponds to the two-dimensional Navier–Stokes equations, which are in turn equivalent to the vorticity equation

$$\frac{\partial \zeta}{\partial t} + \frac{\partial(\psi, \zeta + f)}{\partial(x, y)} = \nu \nabla^2 \zeta \quad (6.3)$$

with

$$\nabla^2 \psi = \zeta. \quad (6.4)$$

For comparison, we solve (6.3) and (6.4) using Arakawa's (1966) energy- and enstrophy-conserving Jacobian and a multigrid elliptic solver.

First we consider nonrotating, infinitely periodic flow in a  $2\pi \times 2\pi$  domain with  $512 \times 512$  grid points. The sound speed  $c = 1$ . The initial condition is random flow with rms velocity (i.e., Mach number) 0.01 and the enstrophy spectrum shown in Fig. 3a. Thus, the time required for fluid particles to traverse the domain at the rms velocity is about 600 time units. Figure 3a shows the enstrophy spectra in the splitting solution and in the Arakawa solution at time  $t = 60$  for the case of *vanishing* viscosity. Such inviscid solutions become increasingly unrealistic as time increases and as enstrophy piles up near the highest resolved wavenumber. However, the intermediate-time comparison in Fig. 3a is useful in that it confirms that the splitting algorithm spuriously accumulates enstrophy at wavenumbers somewhat below the cutoff wavenumber, as suggested by the discussion in section 3.

Figure 3b compares the Arakawa and splitting algorithms at time  $t = 100$  for the case of a nonvanishing viscosity  $\nu = 10^{-5}$  sufficient to fully resolve the dissipation range. The Reynolds number based on the rms velocity and domain size is about 5000. Viscosity destroys the spurious hump in Fig. 3a, but the splitting solution still contains significantly more energy in the viscous dissipation range. The Arakawa and splitting solutions can be brought into closer agreement by minor adjustments to the algorithms—most simply by using a slightly larger viscosity in the splitting algorithm—but here we show only direct comparisons.

Figure 4 compares the vorticity in these same two algorithms for the case of initially overlapping Gaussian vortices of the same sign. Again we take  $\nu = 10^{-5}$ . At time  $t = 100$  (Figs. 4a and 4b) the two vorticity fields are indistinguishable. At time  $t = 300$  (Figs. 4c and 4d)—the time required for fluid particles to traverse half the periodic domain—small differences within the vortex cores become evident, but the two solutions are still remarkably similar. For example, the energies, enstrophies, and maximum velocities differ by less than 1%.

All of these solutions are for the case  $f = 0$  of nonrotating flow. If  $f$  is a nonvanishing constant, it has no effect on the exactly incompressible case governed by (6.3) and (6.4). However, the splitting algorithm (6.1) corresponds to slightly compressible, two-dimensional flow governed

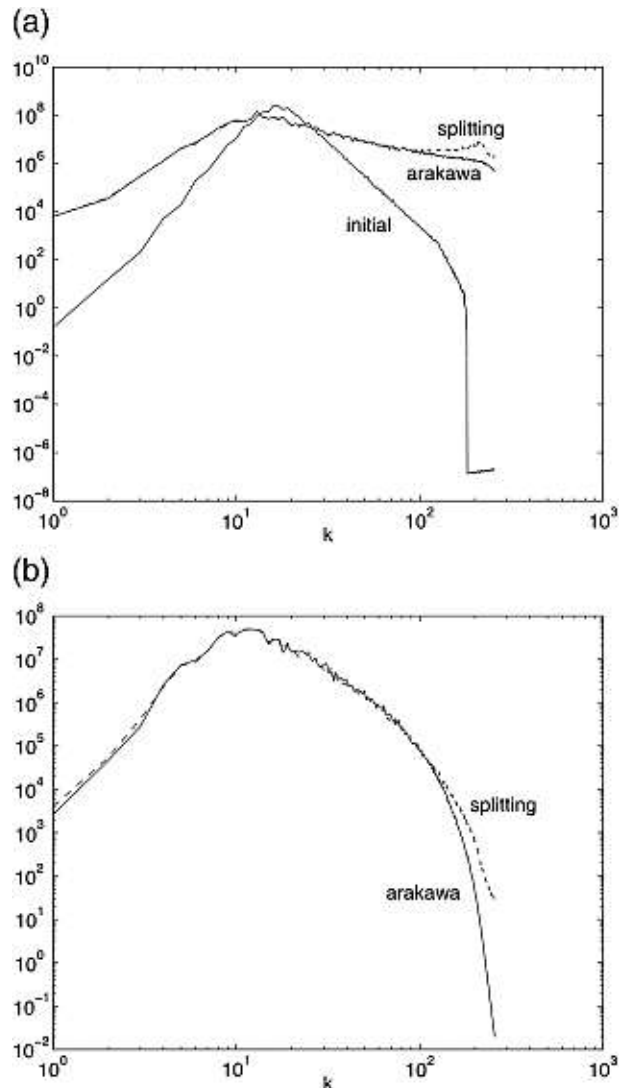


FIG. 3. (a) The enstrophy spectrum corresponding to random initial conditions and the spectra corresponding to inviscid solutions of the Arakawa and splitting algorithms at a time equal to the time required for fluid particles to traverse one-tenth the periodic domain size. (b) The enstrophy spectra in viscous solutions of the Arakawa and splitting algorithms at a time equal to the time required for fluid particles to traverse one-sixth the periodic domain size. The Reynolds number is 5000.

by (2.8). By the analogy between rotating shallow-water dynamics and rotating two-dimensional compressible flow, we expect constant  $f \neq 0$  to produce spurious effects whenever the acoustic deformation radius  $cf$  is less than the domain size. Repeating the experiments shown in Figs. 4a–d for the case  $cf = 2\pi$  of acoustic deformation radius equal to the domain size, we find this difference to be negligible. However, when  $cf$  is much less than the domain size, the Arakawa and splitting solutions differ significantly; for example, Fig. 4e shows the vorticity at

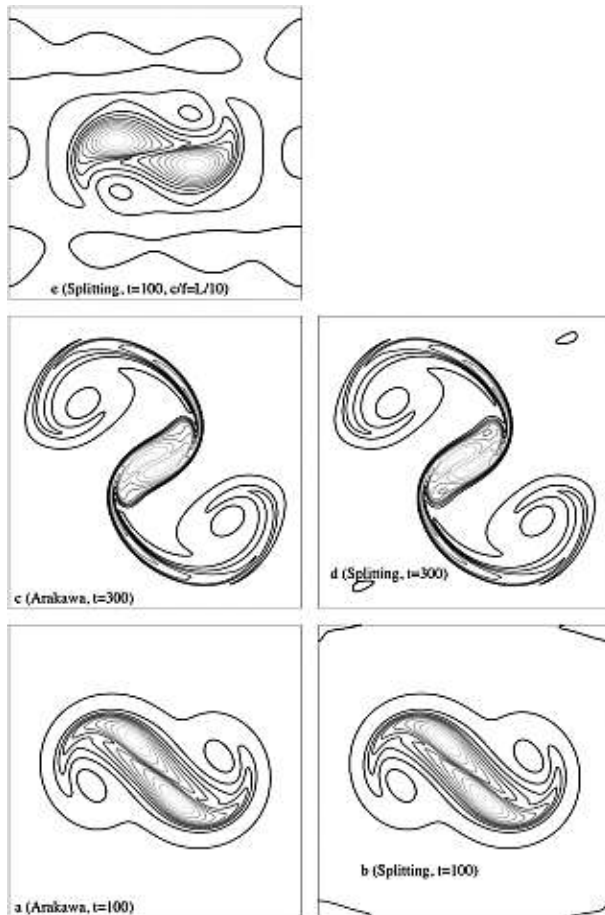


FIG. 4. The merging of two initially overlapping Gaussian vortices as computed by the (a),(c) Arakawa algorithm and (b),(d) the splitting algorithm at times (a),(b)  $t = 100$  and (c),(d)  $t = 300$ . (e) The splitting-algorithm solution at  $t = 100$  with a constant Coriolis parameter chosen to make the acoustic deformation radius equal to one-tenth the periodic domain size. Darker contours correspond to larger values.

$t = 100$  for a splitting-algorithm solution in which  $cf = 2\pi/10$ . The contrast between Fig. 4e and Figs. 4a,b is striking. In the solution corresponding to Fig. 4e, the fluid density departure  $\phi'$  from the mean density  $c^2$  is only about 2%, but the ratio of the “available internal energy”  $\frac{1}{2} \iint d\mathbf{x} (\phi')^2 / c^2$  to the kinetic energy is about 0.5. In all previously described solutions this ratio was less than 0.01. Thus, the requirement  $cf > L$ , where  $L$  is the domain size, is a stringent requirement of our method.

How does this requirement compare to our other requirement that the Mach number be small? In basin-scale ocean modeling, the largest fluid velocities—the largest Mach numbers—occur in western boundary layers. The western boundary layer velocity typically scales as  $U_I L / l$ , where  $U_I$  is the scale for the interior fluid velocity and  $l = \sqrt{U_I / \beta}$  is the inertial western boundary

layer thickness. Assuming that  $f$  is of size  $L\beta$ , the requirement that the Mach number be small in the western boundary layer becomes  $cf > l$ ; the acoustic deformation radius must exceed the western boundary layer thickness. Thus, the previous requirement  $cf > L$  is much more severe: for  $L = 4000$  km the sound speed must exceed  $25\,000$  km day<sup>-1</sup>. Although this is five times smaller than the actual sound speed, it forces the time step to be very small. If, for example, the grid spacing  $\Delta x = 4$  km, then  $\Delta t = \Delta x / c$  is only about 15 s. However, these short time steps are really analogous to individual cycles of the elliptic solver in the more conventional approach. Compared to it, our splitting method offers the advantages of extreme simplicity and massively parallel form.

In the nonrotating experiments described above, the splitting and Arakawa methods seem about equally efficient. In these experiments the maximum velocity (maximum Mach number) never exceeds 0.03. Other experiments show that strong coupling between the hydrodynamic modes and the sound waves does not occur until the Mach number reaches 0.1–0.2. In the nonrotating experiments described above, the splitting-algorithm time step  $\Delta x / c = 2\pi / 512 = 0.012$  is about five times smaller than the time step  $\Delta t = 0.05 \Delta x / u_{\text{rms}}$  used for the Arakawa algorithm. However, the latter requires about 10% more CPU time per unit of simulated time. Most of the time required by the Arakawa algorithm goes to the solution of (6.4). In domains with a complicated, irregular shape, the only practical methods for solving elliptic equations like (6.4) are iterative methods such as multigrid or conjugate gradient. However, such methods are difficult to code in domains with an irregular shape. In contrast, the splitting algorithm is no more difficult to implement in complicated geometry than in simple geometry. One needs only to store the beginning and ending locations of each propagation line.

Figure 5 depicts a splitting-algorithm solution in a two-dimensional domain with an arbitrary shape. Again we take  $c = 1$  and  $\nu = 10^{-5}$ . The domain width is  $O(1)$  and there are  $310^2$  interior grid points. The initial conditions (Fig. 5a) correspond to counterrotating vortices of opposite sign with maximum velocity 0.10. These vortices propel each other toward the irregular boundary, generating large values of vorticity in thin viscous boundary layers that enforce the no-slip condition. By time  $t = 10$  (Fig. 5b) these viscous boundary layers dominate the vorticity field. To keep better track of the interior vorticity, we follow the windowed vorticity (Fig. 5c), obtained by multiplying the window contoured in Fig. 5d by the vorticity in Fig. 5b. The window is a function that varies smoothly between zero on the solid boundary and unity in the interior of the domain. Figure 5e shows the

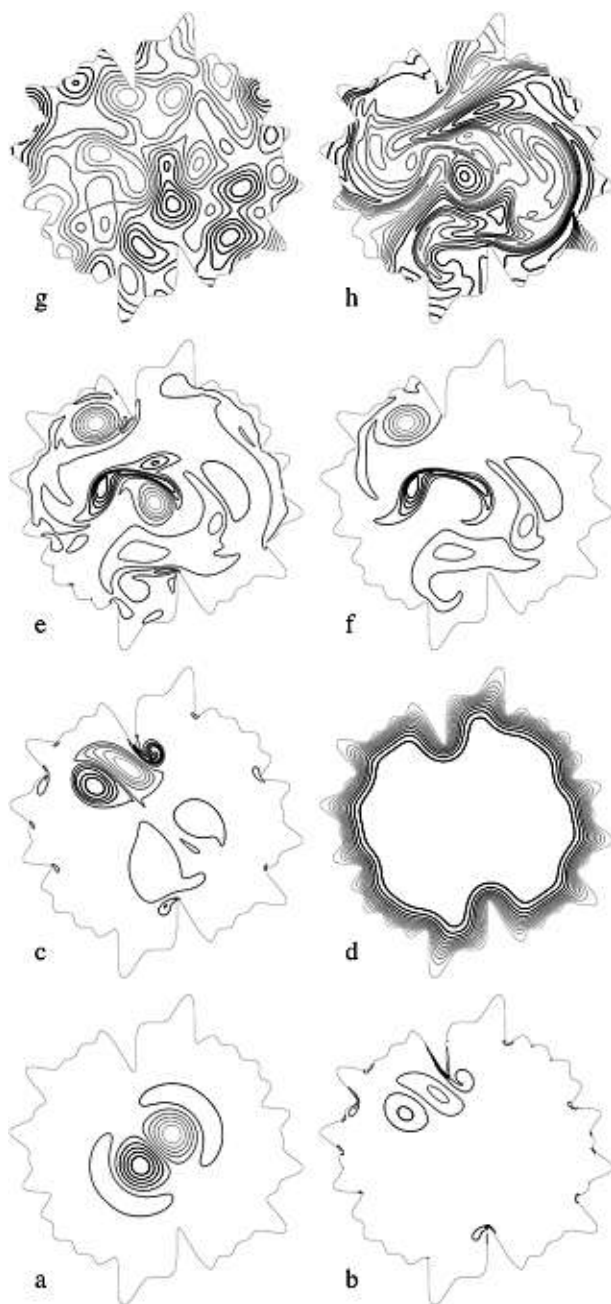


FIG. 5. Splitting-algorithm solution of counterrotating vortices in an arbitrarily shaped domain with no-slip boundaries. By time  $t = 10$  (a) the initial vorticity has evolved to (b) the state in which viscous boundary layers dominate. The windowed vorticity, obtained by multiplying the field in (b) by the (d) window, reveals (c) the interior pattern. (e) The windowed vorticity at  $t = 30$  and (f) a passive scalar initially equal to the vorticity at the same time. An initially random passive scalar at (g)  $t = 0$  and (h)  $t = 30$  in the same flow. Darker contours correspond to large values.

windowed vorticity at  $t = 30$ , by which time the maximum fluid velocity has fallen to 0.044. For comparison, Fig. 5f shows a passive scalar field  $\theta$  that is initially set equal to the vorticity. Although the scalar has a diffusivity equal to the fluid viscosity, Figs. 5e and 5f differ significantly because of the huge difference in boundary conditions: no flux for the scalar versus no slip for the vorticity. Nevertheless, the similarity between Figs. 5e and 5f in the fluid interior shows that the vorticity there is carried on fluid particles (apart from the effects of viscosity). We solve for  $\theta$  with the splitting sequence

$$T_x T_y D_x D_y D_y D_x T_y T_x, \quad (6.5)$$

where  $T_x$  and  $T_y$  are the buoyancy splits defined in section 4, and  $D_x$  and  $D_y$  are diffusion splits similar to (6.2) but acting only in the  $x$  and  $y$  directions, respectively, and incorporating the boundary conditions of no scalar flux through the boundary (because of the no-flux boundary conditions, it is simplest to split the diffusion into its directional components). Since neither  $T_x$  nor  $T_y$  contains buoyancy force,  $\theta$  is a passive scalar and the various splits in (6.5), each of which acts for a time  $\Delta x/c$ , need not be sandwiched within (6.1). In practice, we alternate between (6.1) and (6.5). Finally, in this same flow field, we consider a passive scalar with the random initial conditions shown in Fig. 5g. The scalar field at  $t = 30$  (Fig. 5h) shows how (6.5) accommodates the no-flux boundary conditions.

It remains to consider solutions containing buoyancy force. This we do in section 8, but first we address a fundamental difficulty that affects ocean circulation models of all kinds.

## 7. The aspect-ratio trick

The typical horizontal resolution in ocean general circulation models has increased enormously: the horizontal grid spacing  $\Delta x$  is now sometimes as small as a few kilometers. However, this is still much larger than the typical vertical grid spacing  $\Delta z$  of a few tens of meters. The huge disparity between these scales is the source of many difficulties. To cite but one example, open ocean convection occurs in plumes that are no wider than they are deep. The models cannot resolve these plumes. Moreover, because the plumes occur on the scale of fastest growth for convective instability, the model convection occurs at the smallest resolved horizontal scales—a recipe for numerical noise. In practice, eddy viscosity damps out the convective instability and an explicit, but quite arbitrary, vertical mixing relieves static instability.

Browning et al. (1990) proposed that the vertical component of the Boussineq momentum equation (2.17a) be replaced by

$$\frac{1}{\mu^2} \frac{Dw}{Dt} = -\frac{\partial\phi}{\partial z} + \theta \tag{7.1}$$

in which  $\mu = \Delta z/\Delta x \ll 1$  is a small parameter. The standard Boussinesq equations correspond to  $\mu = 1$ . The modification (7.1) increases the vertical inertia by a vast amount, but not so much as to upset hydrostatic balance at large scales of motion. As pointed out by Newberger and Allen (1996) and Salmon (1999b), the modification (7.1) is equivalent to erasing the factor of aspect-ratio-squared that precedes the vertical acceleration when the Boussinesq equations are written in standard nondimensional form. This ‘‘aspect ratio trick,’’ which has been independently rediscovered by several authors, was originally designed only to allow longer time steps. However, as one of several bonuses, this trick increases the horizontal scale of interior convection and the thickness of sidewall boundary layers to the point where they are resolved by the model. The aspect-ratio trick is close in spirit to our treatment of sound waves: just as we loosen the incompressibility constraint—decrease the sound speed—to allow longer time steps, the modification  $\mu \ll 1$  loosens the hydrostatic constraint to the same purpose.

Newberger and Allen (1996) compare numerical solutions using (7.1) with very small values of  $\mu$  to solutions of the standard Boussinesq equations with  $\mu = 1$ . They find significant differences. However, their test cases have a relatively high horizontal resolution: the typical domain width is 60 km. In such cases, the standard Boussinesq equations can be accurately solved. In basin-scale calculations the choice is between severely underresolving the exact physics, on the one hand, and accurately solving the modified physics, on the other. In this paper, we choose the latter. However, as in Salmon (1999b), our basic motivation is a desire to make sound waves propagate one vertical grid spacing in the same time required to propagate one horizontal grid spacing. Thus, if  $c$  is the horizontal sound speed, we take the vertical sound speed to be  $\mu c$ .

The modification (7.1) is equivalent to the following changes to the algorithm described in previous sections. First, we replace the vertical part of the sound-wave bracket (2.12b) by

$$\{F, H\}_2 = \mu^2 c^2 \iiint d\mathbf{x} \left( \frac{\delta H}{\delta w} \frac{\partial}{\partial z} \frac{\delta F}{\delta \phi} - \frac{\delta F}{\delta w} \frac{\partial}{\partial z} \frac{\delta H}{\delta \phi} \right). \tag{7.2}$$

Second, we replace the vertical part of the buoyancy bracket (2.12c) by

$$\{F, H\}_3 = \mu^2 c^2 \iiint d\mathbf{x} \frac{\alpha}{\phi} \left( \frac{\delta H}{\delta w} \frac{\partial}{\partial z} \frac{\delta F}{\delta \alpha} - \frac{\delta F}{\delta w} \frac{\partial}{\partial z} \frac{\delta H}{\delta \alpha} \right). \tag{7.3}$$

Third, in the rotation bracket (2.12a) we replace the relative vorticity

$$\begin{aligned} \boldsymbol{\omega} &= \nabla \times \mathbf{v} = (w_y - v_z, u_z - w_x, v_x - u_y) \\ &\rightarrow (w_y - \mu^2 v_z, \mu^2 u_z - w_x, v_x - u_y) \\ &\equiv (\omega^x, \omega^y, \omega^z). \end{aligned} \tag{7.4}$$

Finally, we replace the Hamiltonian (2.13) by

$$H = \iiint d\mathbf{x} \left( \frac{1}{2} u^2 + \frac{1}{2} v^2 + \frac{1}{2} \frac{w^2}{\mu^2} + \frac{1}{2} \frac{\phi^2}{c^2} - \alpha z \right). \tag{7.5}$$

The effect of these changes is to replace the vertical sound-wave split by

$$\frac{\partial w}{\partial t} = -\mu^2 \frac{\partial \phi}{\partial z}, \quad \frac{\partial \phi}{\partial t} = -c^2 \frac{\partial w}{\partial z}, \quad \frac{\partial(\phi\theta)}{\partial t} = 0; \tag{7.6}$$

the vertical buoyancy split by

$$\frac{\partial w}{\partial t} = \mu^2 \theta, \quad \frac{\partial \phi}{\partial t} = 0, \quad \frac{\partial}{\partial t} \left( \frac{\phi\theta}{c^2} \right) = -\frac{\partial}{\partial z} (w\theta); \tag{7.7}$$

and the two horizontal rotation splits by

$$\frac{\partial u}{\partial t} = 0, \quad \frac{\partial v}{\partial t} = \frac{c^2}{\phi} \omega^x \frac{w}{\mu^2}, \quad \frac{\partial w}{\partial t} = -\frac{c^2}{\phi} \mu^2 \omega^x v; \tag{7.8}$$

$$\frac{\partial u}{\partial t} = -\frac{c^2}{\phi} \omega^y \frac{w}{\mu^2}, \quad \frac{\partial v}{\partial t} = 0, \quad \frac{\partial w}{\partial t} = \frac{c^2}{\phi} \omega^y u; \tag{7.9}$$

where the modified vorticity components are defined in (7.4). The energy-conserving solutions of (7.8) and (7.9), analogous to (5.3), are

$$\begin{aligned} v(t) &= v(0) \cos(\gamma_x) + \frac{w(0)}{\mu} \sin(\gamma_x), \\ \frac{w(t)}{\mu} &= \frac{w(0)}{\mu} \cos(\gamma_x) - v(0) \sin(\gamma_x), \end{aligned}$$

where

$$\gamma_x \equiv \frac{\omega_x(0)}{\mu} t c^2 / \phi \tag{7.10}$$

and

$$\begin{aligned} u(t) &= u(0) \cos(\gamma_y) - \frac{w(0)}{\mu} \sin(\gamma_y), \\ \frac{w(t)}{\mu} &= \frac{w(0)}{\mu} \cos(\gamma_y) + u(0) \sin(\gamma_y), \end{aligned}$$

where

$$\gamma_y \equiv \frac{\omega_y(0)}{\mu} t c^2 / \phi. \tag{7.11}$$

The vertical rotation split  $R_z$  is unaffected. We approximate the rotation splits (7.10) and (7.11) in the same manner as (5.4). If  $\mu < 1$ , the split (7.10) rotates the vector  $(v, w)$  in an ellipse of aspect ratio  $\mu$ . In the limit  $c \rightarrow \infty$ , the complete modified dynamics,

$$\frac{\partial u}{\partial t} = \frac{c^2}{\phi} \left[ -\mathbf{v} \cdot \nabla u + \frac{1}{2} \frac{\partial}{\partial x} (u^2 + v^2 + w^2/\mu^2) \right] - \frac{\partial \phi}{\partial x}, \quad (7.12a)$$

$$\frac{\partial v}{\partial t} = \frac{c^2}{\phi} \left[ -\mathbf{v} \cdot \nabla v + \frac{1}{2} \frac{\partial}{\partial y} (u^2 + v^2 + w^2/\mu^2) \right] - \frac{\partial \phi}{\partial y}, \quad (7.12b)$$

$$\frac{\partial w}{\partial t} = \frac{c^2}{\phi} \left[ -\mathbf{v} \cdot \nabla w + \frac{\mu^2}{2} \frac{\partial}{\partial z} (u^2 + v^2 + w^2/\mu^2) \right] - \mu^2 \frac{\partial \phi}{\partial z} + \mu^2 \theta, \quad (7.12c)$$

$$\frac{\partial \phi}{\partial t} = -c^2 \nabla \cdot \mathbf{v}, \quad (7.12d)$$

and

$$\frac{\partial}{\partial t} \left( \frac{\phi}{c^2} \theta \right) = -\nabla \cdot (\mathbf{v} \theta), \quad (7.12e)$$

limit on the standard Boussinesq equations (2.17) except that the vertical momentum equation is replaced by (7.1). In particular, a scale analysis shows that (7.12e) approximates (2.17c) when the scale depth  $c/N$  is much greater than the fluid depth  $H$ , where  $N$  is the scale for the Väisälä frequency. Thus, if the horizontal domain size  $L$  is much greater than the internal deformation radius  $NH/f$ , the most stringent requirement on sound speed is  $cf \gg L$ .

## 8. Ocean section experiments

To test the buoyancy split and the modifications proposed in the previous section, we consider rotating  $y$ -independent flow in the  $x$ - $z$  plane. As  $c \rightarrow \infty$ , the dynamics (7.12) (with viscous and diffusive terms added) limits on

$$\left[ \frac{\partial}{\partial t} - A_h(\partial_{xx} + \partial_{yy}) - A_v \partial_{zz} \right] u = -\frac{\partial(\psi, u)}{\partial(x, z)} + fv - \frac{\partial \phi}{\partial x}, \quad (8.1a)$$

$$\left[ \frac{\partial}{\partial t} - A_h(\partial_{xx} + \partial_{yy}) - A_v \partial_{zz} \right] v = -\frac{\partial(\psi, v)}{\partial(x, z)} - fu, \quad (8.1b)$$

$$\left[ \frac{\partial}{\partial t} - A_h(\partial_{xx} + \partial_{yy}) - A_v \partial_{zz} \right] w = -\frac{\partial(\psi, w)}{\partial(x, z)} + \mu^2 \left( -\frac{\partial \phi}{\partial z} + \theta \right), \quad (8.1c)$$

and

$$\left[ \frac{\partial}{\partial t} - K_h(\partial_{xx} + \partial_{yy}) - K_v \partial_{zz} \right] \theta = -\frac{\partial(\psi, \theta)}{\partial(x, z)}, \quad (8.1d)$$

where  $\psi$ , defined by  $u = -\psi_z$  and  $w = \psi_x$ , is the streamfunction for the flow in the  $x$ - $z$  plane and  $A_h, A_v, K_h$ , and  $K_v$  are horizontal and vertical eddy viscosity and diffusion coefficients. We solve (8.1) by the algorithm

$$D_{xz} R_x R_y R_z T_x S_x S_z T_z T_z S_z S_x T_x R_z R_y R_x D_{xz}, \quad (8.2)$$

where  $D_{xz}$  represents both the viscosity and diffusion splits. All the splits in (8.2) act for the time  $\Delta x/c = \Delta z/\mu c$ . The viscosity split incorporates the prescribed wind stress and the no-slip boundary conditions at solid boundaries. The diffusion split incorporates surface heat flux and the no-flux boundary conditions at solid boundaries. All the other splits retain the conservation properties described in previous sections. The computational domain (e.g., Fig. 6) is the east–west section with rugged bathymetry and maximum depth  $H = 1.08$  km between the southern tip of San Clemente Island and the site of our computations at La Jolla, California, a distance  $L = 101.4$  km to the east. Besides the specified geometry and the forcing/initial conditions, the only parameters of the model are the horizontal grid spacing  $\Delta x$ , the vertical grid spacing  $\Delta z$ , the sound speed  $c$ , and the eddy coefficients  $A_h, A_v, K_h$ , and  $K_v$ .

Idealized, flat-bottom, homogeneous-fluid solutions were found to agree closely with linear boundary layer theory provided that the acoustic deformation radius  $cf$  was sufficiently large and boundary layers were well resolved. In particular, the interior northward velocity agrees with the theoretical prediction  $v_I = \sqrt{2} \tau \sqrt{f} A_v$  to within 0.01% when  $cf = 10L$ , when the sidewall (i.e., Stewartson) boundary layer thickness  $\delta_{St} \equiv (A_h L/f)^{1/3}$  is at least  $4\Delta x$ , and when the Ekman boundary layer thickness  $\delta_{Ek} \equiv (A_v/f)^{1/2}$  is at least  $4\Delta z$ . When  $cf = 2L$ , this error increased to 5.3%. When  $\delta_{Ek} = 2\Delta z$ , this error increased to 3.0%. In all the calculations to be presented, we take  $cf = 10L$ . Since our coarsest-resolution experiments correspond to  $\Delta x = 510$  m and  $\Delta z = 5.43$  m, we choose  $A_h = 6.69 \text{ m}^2 \text{ s}^{-1}$  to make  $\delta_{St} = 4 \times 510$  m, and we choose  $A_v = 3.715 \times 10^{-2} \text{ m}^2 \text{ s}^{-1}$  to make  $\delta_{Ek} = 4 \times 5.43$  m. For the diffusion coefficients we take  $K_h = A_h$

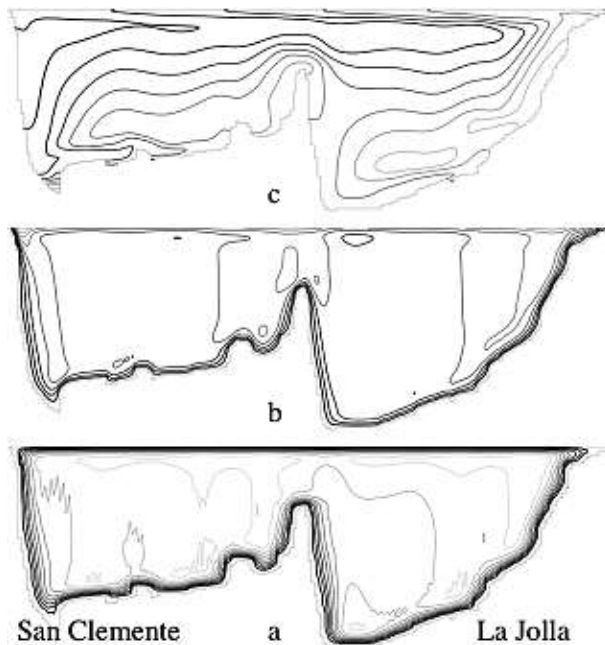


FIG. 6. The (a) streamfunction, (b) northward velocity, and (c) “buoyancy” in an east–west section between San Clemente Island on the left and La Jolla on the right. In this experiment the buoyancy force is switched off, thus (c) depicts a passive scalar  $\theta$  for which  $d\theta/dz$  is initially a constant. The flow, driven by a uniform southward wind stress of magnitude  $1 \text{ cm}^2 \text{ s}^{-2}$ , is westward in the surface Ekman layer and eastward in the bottom Ekman layer. The maximum  $u$ ,  $v$ , and  $w$  are  $3.46$  and  $20.9 \text{ km day}^{-1}$  and  $57.6 \text{ m day}^{-1}$ , respectively. At the time shown (50 days after a state of rest) the velocity field is steady. Darker contours correspond to larger values.

and  $K_v = 5.0 \times 10^{-4} \text{ m}^2 \text{ s}^{-1}$ . We use these same values in all the experiments discussed.

All of these eddy coefficients are somewhat larger than the values typically used for the interior regions of ocean circulation models. Here, as is normally done there, it would be possible to allow these coefficients to vary between relatively large values in the boundary layers and much smaller values in the ocean interior. However, in this initial study, it was thought best to keep the number of parameters to an absolute minimum by allowing only constant values for the eddy coefficients.

We discuss only a few of many dozens of experiments performed. Because nothing varies in the  $y$  direction, our solutions cannot be realistic; they serve only to demonstrate model behavior. Figures 6 and 7 show the streamfunction  $\psi$ , the northward flow  $v$ , and the buoyancy  $\theta$  at time  $t = 50$  days in solutions that begin from a state of rest and uniform stratification  $d\theta/dz$ . The initially uniform stratification corresponds to a change of one unit of  $\sigma_\theta$  ( $1 \sigma$  unit) from deepest ocean bottom to the ocean surface. In both solutions,  $\Delta x = 510 \text{ m}$  and

$\Delta z = 5.43 \text{ m}$ , corresponding to a maximum of 200 grid points in each direction. In the solution of Fig. 6, the buoyancy force has been turned *off*; thus  $\theta$  is a passive scalar. In the solution of Fig. 7, the buoyancy force is *on*. Both solutions are driven by a uniform southward wind stress  $\tau^y = -1 \text{ cm}^2 \text{ s}^{-2}$ . In both solutions, the southward wind stress drives a strong westward flow in the surface Ekman layer. In the homogeneous fluid solution of Fig. 6, downwelling near San Clemente Island feeds a bottom Ekman layer in which the flow returns to the mainland. In the solution of Fig. 7, the stratification resists downwelling and a stronger flow closes at intermediate depth. A density inversion caused by the strong westward flow in the upper Ekman layer produces a weak convective cell in Fig. 7c. The oscillations in Figs. 6a and 7a are sound waves generated by the flow impinging on San Clemente Island. They disappear as the resolution or the horizontal viscosity is increased.

Figures 8 and 9 show solutions designed to test the performance of the model when buoyancy forces are strong. The initial condition is a statically unstable state of rest with  $\phi \equiv c^2$  and

$$\theta = -\theta_0 \exp(-z/100\text{m}), \quad (8.3)$$

where the amplitude  $\theta_0$  corresponds to  $0.10 \sigma$  units. In this case the model rapidly adjusts to a state of hydrostatic balance by generating sound waves. It is possible to avoid this brief adjustment phase by choosing the initial pressure to be in hydrostatic balance with the initial buoyancy, but it seems simpler to let the sound waves do their work. In any case, the sound waves are quickly overwhelmed by the much larger convective motions of primary interest.

The solution of Fig. 8 has the same spatial resolution as the experiments shown in Figs. 6 and 7, corresponding to a maximum of 200 grid points in both directions. In the solution of Fig. 9, the horizontal grid spacing has been reduced from  $\Delta x = 510 \text{ m}$  to  $\Delta x = 204 \text{ m}$ , corresponding to a maximum of 500 grid points in the horizontal direction. Because of the aspect-ratio trick, convective instability is well resolved in both Figs. 8 and 9. However, there is a real, physical difference between these two solutions because they correspond to different values of  $\mu$  ( $0.0106$  and  $0.0267$  in Figs. 8, 9, respectively). Once again, exact Boussinesq dynamics corresponds to  $\mu = 1$  and is achieved only by allowing  $\Delta x = \Delta z$ . Because of the increased resolution, the convection is stronger and proceeds more rapidly in Fig. 9 than in Fig. 8. The times in the two figures have been chosen to represent the flows at similar stages of development. At the time corresponding to Fig. 8d, the vertical rms velocity is  $88.9 \text{ m day}^{-1}$ ; in Fig. 9d it is  $224 \text{ m day}^{-1}$ . In

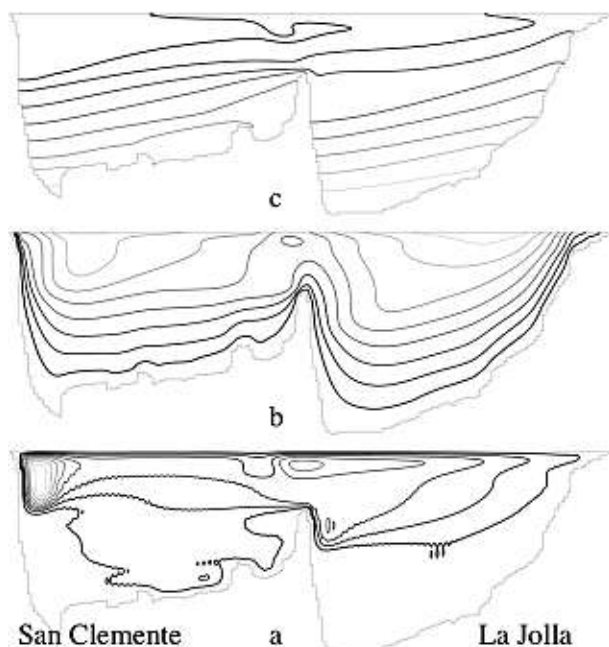


FIG. 7. As in Fig. 6, but with the buoyancy force turned on. The uniform initial stratification corresponds to a difference of  $1 \sigma$  unit between the ocean surface and deepest ocean bottom. The stratification concentrates the flow in the upper ocean, hence the maximum  $u$ ,  $v$ , and  $w$  ( $4.81$  and  $59.8 \text{ km day}^{-1}$  and  $131 \text{ m day}^{-1}$ , respectively) are larger than in Fig. 6. Static instability in the upper Ekman layer generates a small convective cell at midbasin. Darker contours correspond to larger values.

both figures, convection occurs fastest near the two coastlines. Our method easily accommodates the rapid descent of dense water along the rough, stair-step topography.

## 9. Discussion

The key features of our model are its extreme simplicity and its massively parallel form. Each of the propagators in (8.1) represents a simple operation. For example, each of the sound-wave propagators,  $S_x$ ,  $S_y$ , and  $S_z$ , which merely shift Riemann invariants left and right, corresponds to a computer subroutine with only 26 lines of FORTRAN. The other propagators are comparably simple. Both the sound-wave and buoyancy propagators  $T_x$ ,  $T_y$ , and  $T_z$  operate along propagation lines that require no elaborate treatment of the boundaries. At the beginning of the calculation, one must use the bathymetric data to determine the beginning and ending location of each propagation line but, once these locations are stored, very complicated boundary shapes require no more operations than very simple ones. The rotation propagators  $R_x$ ,  $R_y$ , and  $R_z$  operate on interior fluid points independently. Thus, every propagation line

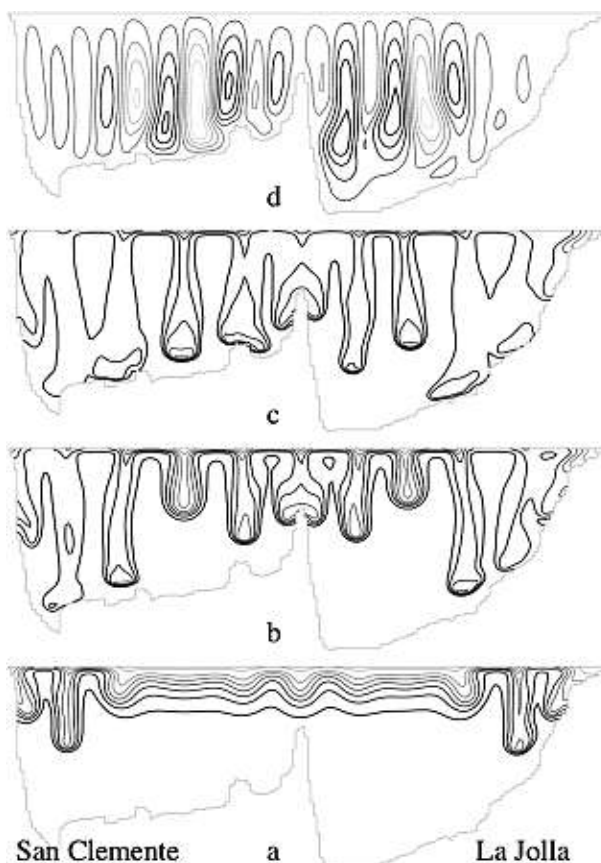


FIG. 8. The buoyancy at (a) 14 days, (b) 18 days, and (c) 20 days and (d) the streamfunction at 20 days in an experiment beginning at a state of rest and the unstable stratification (8.3). The grid spacings are  $\Delta x = 510 \text{ m}$  and  $\Delta z = 5.43 \text{ m}$ , corresponding to a maximum of 200 grid points in each direction. At the final time, the maximum eastward, northward, and vertical speeds are  $5.65$  and  $21.4 \text{ km day}^{-1}$  and  $268 \text{ m day}^{-1}$ , respectively.

in the case of the sound and buoyancy propagators, and every interior point in the case of the rotation propagators, could be sent to a different processor. The forcing and dissipation propagators could be handled in the same way. To maintain load balance among the processors, one could sort the propagation lines by their length and then process lines of similar length simultaneously. The sorting of propagation lines need only be done once (for each of the three directions) at the beginning of the computation.

The tremendous advantage of massively parallel form should easily compensate for the primary disadvantage of our model: the very short time cycle required to satisfy the condition that the acoustic deformation radius  $c/f$  be larger than the domain size. For a domain size of, say,  $4000 \text{ km}$  and a horizontal grid spacing of  $\Delta x = 5 \text{ km}$ , the sound speed must exceed  $25\,000 \text{ km day}^{-1}$  and the time cycle  $2\Delta x/c$  must be less than  $1/2 \text{ min}$ . While this

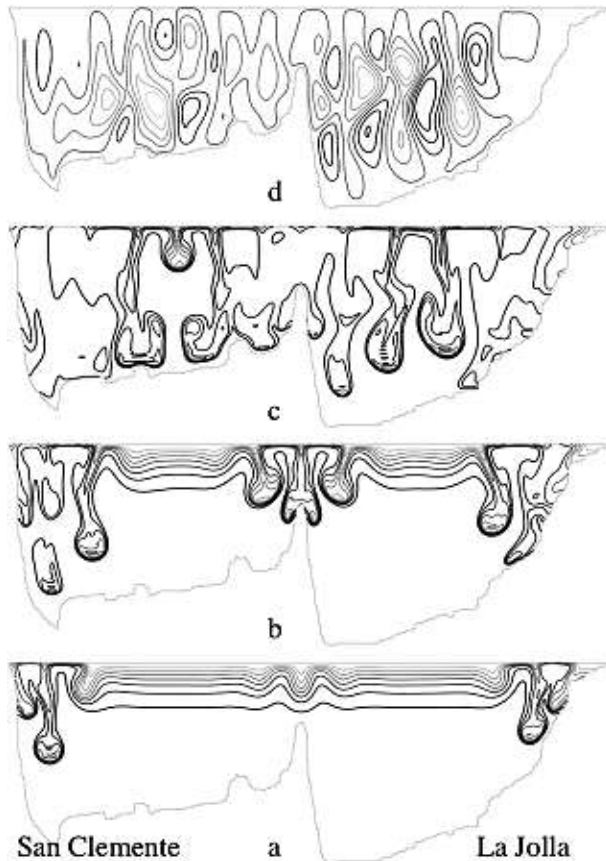


FIG. 9. The buoyancy at (a) 5 days, (b) 6 days, and (c) 8 days and (d) the streamfunction at 8 days in an experiment beginning at the same statically unstable initial state as shown in Fig. 8. The only difference between this experiment and that shown in Fig. 8 is that the horizontal grid spacing has been reduced to  $\Delta x = 204$  m, corresponding to 500 grid points in the east–west direction. At the final time, the maximum eastward, northward, and vertical speeds are  $16.5$  and  $30.9$  km day $^{-1}$  and  $837$  m day $^{-1}$ , respectively.

sound speed is still about five times smaller than the actual sound speed, such time steps are, indeed, very short. These short time steps should be compared not to the time steps in conventional models but to the iteration steps required to solve elliptic equations at fixed times; however, the iteration steps are not as easy to program in parallel form.

Although our complete model is somewhat novel, none of its key ingredients is completely new. For example, operator splitting (sometimes called fractional steps) has been tried by many authors (see, e.g., Skamarock 2006). However, our splitting method violates a frequently cited rule of conventional operator splitting that makes our method much more akin to the lattice Boltzmann method. In conventional splitting, one normally avoids separating fundamental physical balances into different splits. In our model, geostrophic balance is spread

among  $S_x$  and  $S_y$ , which contain the horizontal pressure gradient, and  $R_z$ , which contains the Coriolis force. Similarly, hydrostatic balance is spread between  $S_z$ , which contains the vertical pressure gradient, and  $T_z$ , which contains the buoyancy force. If one analyzes the subsequence  $S_z T_z T_z S_z$  of (8.2) in the manner of section 3, one finds a static (zero frequency) eigenvector corresponding to hydrostatic balance. This static eigenvector has vanishing vertical velocity at all wavenumbers. The existence of such a zero-velocity eigenvector is somewhat remarkable when one considers that  $S_z T_z T_z S_z$  achieves hydrostatic balance by alternately accelerating fluid particles in  $T_z$  and then decelerating them in  $S_z$ . In fact, the individual components  $S_z T_z$  and  $T_z S_z$  each have static eigenvectors corresponding to physical states with *nonzero* vertical velocities. Thus, Strang splitting of the propagators is essential to our method.

However, the time stepping error associated with Strang splitting is the primary source of model inaccuracy. In fact, the buoyancy split is the only split (besides dissipation) in which spatial truncation error is even an issue. This spatial truncation error could be reduced by using a more accurate form of (4.5), but the Strang-splitting error could not be eliminated without sacrificing the model’s key advantages. The error associated with Strang splitting of the subsequence  $S_x S_y S_y S_x$  was analyzed in section 3. Analysis of the subsequence  $S_z T_z T_z S_z$  yields similar results. One finds that the smallest resolved wavelength (two grid distances) is severely misrepresented, but motions at twice this minimum wavelength contain errors of only about 10%. Hence, the smallest resolved wavelengths must be kept well inside the dissipation range.

Even in conventional grid models, the most poorly resolved waves misbehave. The question, then, is whether this is more of a problem in the proposed method than in conventional models. The evidence suggests that it is more of a problem—but not much more. For example, if one looks closely at Figs. 4c and 4d, which correspond to the Arakawa and splitting algorithms, respectively, with the same spatial resolution, one sees that the vortex cores in Fig. 4d contain small-scale oscillations that are probably noise. As stated in section 6, this disagreement disappears if the viscosity is increased. Of course, increasing the viscosity sacrifices spatial resolution.

It is important to emphasize that our proposed method is closely related to lattice Boltzmann methods and that lattice Boltzmann methods lie at the opposite end of the trade-off curve from conventional models containing numerous logical branches and other refinements. In lattice Boltzmann models, mindlessly simple operations are repeated with mind-numbing

frequency. At least slightly greater spatial resolution may be required to achieve the same accuracy as in conventional models, but the potential for efficient parallel processing is much greater. Our method differs from pure lattice Boltzmann models in that we use the lattice Boltzmann approach only for the sound-waves split. Pure lattice Boltzmann models solve the complete dynamics with particle-hopping operations. To incorporate the advective momentum flux, the particles must hop in diagonal directions and this seems to be the bane of using the pure lattice Boltzmann methods in ocean models in which the physics itself is very different in the vertical and horizontal directions. In this paper, we combine the most attractive properties of the lattice Boltzmann approach with useful properties of the conventional approaches.

Chief among these useful properties is the ability to maintain at least some conservation laws. Although the analytical dynamics (2.11)–(2.13) conserve all the invariants (2.18), our model equations conserve, or semi-conserve, only that subset of invariants noted in the preceding sections. (Since, as explained in section 7, the aspect-ratio trick is equivalent to a formal rescaling of the vertical coordinate, it alters but does not destroy conservation laws.) In particular, our model equations do not conserve potential vorticity. However, the retained conservation laws—mass, energy, buoyancy, and buoyancy squared—lend our method great stability. When breakdown occurs, it is always because the local Mach number becomes too high. The breakdown consists of a spurious local generation of sound waves. In fact, relatively vigorous sound waves are always present but, if the sound speed is sufficiently large (i.e., if the time step is sufficiently small), then the sound waves are negligible in comparison to the slow hydrodynamic motions of fundamental interest.

Our method could not easily be applied to nonuniform grids. To maintain the important feature that sound waves move one grid distance in a time step, the sound speed would need to vary with location. The time step would then be determined by the need to keep the Mach number small in the regions of highest spatial resolution. For such a small time step, one might as well enjoy the accuracy and simplicity of a uniformly high-resolution model. Although it is somewhat jarring to imagine an ocean model in which the vertical spacing between grid points is everywhere the same, this apparent wastefulness is compensated by the stark simplicity of the computer code and the potential for efficient parallel processing.

Could the proposed method really be more efficient than the methods currently in use? This question can only be answered by actual calculations involving large

irregularly shaped three-dimensional domains on massively parallel computing platforms. However, some tentative answers will be ventured. If one is strictly interested in hydrostatic modeling—for which the conventional approach is to solve a two-dimensional elliptic problem or to separately time step a fast external-gravity wave system—then the proposed method is relatively inefficient. However, there are good reasons to anticipate the widespread use of nonhydrostatic dynamics. In fact, this paper actually advocates the exaggeration of nonhydrostatic effects. That is, instead of delaying the incorporation of nonhydrostatic physics until increases in horizontal resolution make it absolutely necessary, we propose to accelerate this incorporation by means of the “aspect-ratio trick,” adopting a physics in which the smallest horizontal scales are always nonhydrostatic. The aspect-ratio trick allows us to apply each of our propagators exactly twice in a time cycle. At the same time, the trick addresses a fundamental difficulty shared by all ocean circulation models, associated with the scale separation between the horizontal and vertical directions. Conventional approaches to this difficulty include subgrid-scale closures that explicitly mix buoyancy to neutral stability and greatly enhanced vertical mixing coefficients in regions of static instability.

Although this paper reports only two-dimensional solutions, a three-dimensional version of the model has been tested at the relatively low resolution of  $100^3$ . Much more testing is required. However, it appears that the generalization from two to three space dimensions requires no new ideas or methods beyond those presented here.

*Acknowledgments.* This work was supported by National Science Foundation Grant OCE-0542890. I gratefully acknowledge very helpful comments from Christopher Wolfe, Paul Dellar, and two anonymous referees.

#### REFERENCES

- Arakawa, A., 1966: Computational design for long-term numerical integration of the equations of fluid motion: Two-dimensional incompressible flow. Part I. *J. Comput. Phys.*, **1**, 119–143.
- Browning, G. L., W. R. Holland, H.-O. Kreiss, and S. J. Worsley, 1990: An accurate hyperbolic system for approximately hydrostatic and incompressible oceanographic flows. *Dyn. Atmos. Oceans*, **14**, 303–332.
- Durran, D. R., 1999: *Numerical Methods for Wave Equations in Geophysical Fluid Dynamics*. Springer, 465 pp.
- Newberger, P. A., and J. S. Allen, 1996: On the use of the Boussinesq equations, the reduced system, and the primitive equations for the computation of geophysical flows. *Dyn. Atmos. Oceans*, **25**, 1–24.

- Salmon, R., 1999a: The lattice Boltzmann method as a basis for ocean circulation modeling. *J. Mar. Res.*, **57**, 503–535.
- , 1999b: Lattice Boltzmann solutions of the three-dimensional planetary geostrophic equations. *J. Mar. Res.*, **57**, 847–884.
- , 2004: Poisson-bracket approach to the construction of energy- and potential-enstrophy-conserving algorithms for the shallow-water equations. *J. Atmos. Sci.*, **61**, 2016–2036.
- , 2005: A general method for conserving quantities related to potential vorticity in numerical models. *Nonlinearity*, **18**, R1–R16.
- , 2007: A general method for conserving energy and potential enstrophy in shallow-water models. *J. Atmos. Sci.*, **64**, 515–531.
- Shepherd, T. G., 1990: Symmetries, conservation laws, and Hamiltonian structure in geophysical fluid dynamics. *Advances in Geophysics*, Vol. 32, Academic Press, 287–338.
- Skamarock, W. C., 2006: Positive-definite and monotonic limiters for unrestricted-time-step transport schemes. *Mon. Wea. Rev.*, **134**, 2241–2250.
- Suzuki, M., 1992: General nonsymmetric higher-order decomposition of exponential operators and symplectic integrators. *J. Phys. Soc. Japan*, **61**, 3015–3019.